Influence of Silica Coatings on Magnetite-Catalyzed Selenium Reduction

Sara Goberna-Ferrón, Maria Asta, Bahareh Zareeipolgardani, Sarah Bureau, Nathaniel Findling, Laura Simonelli, Jean-Marc Greneche, Laurent Charlet, A Fernandez-Martinez

Influence of silica coatings on magnetite-catalyzed selenium reduction

*Sara Goberna-Ferrón[1, †, *], Maria P. Asta[2], Bahareh Zareeipolgardani[1], Sarah Bureau[1], Nathaniel Findling[1], Laura Simonelli[3], Jean-Marc Greneche[4], Laurent Charlet[1], Alejandro Fernández-Martínez[1, *]*

[1] Univ. Grenoble Alpes, Univ. Savoie Mont Blanc, CNRS, IRD, IFSTTAR, ISTerre, 38000 Grenoble, France

[2] Institute of Earth Surface Dynamics, Faculty of Geosciences and Environment, University of Lausanne, 1015 Lausanne, Switzerland

[3] BL22–CLÆSS: Core Level Absorption and Emission Spectroscopies Beamline–Experiments Division, ALBA Synchrotron Light Source, Ctra. BP 1413 km. 3,3 08290 Cerdanyola del Vallès, Barcelona, Spain

[4] Institut des Molécules et Matériaux du Mans (IMMM) CNRS UMR-6283, Le Mans Université, Le Mans, F-72085, France

KEYWORDS. Sorption, Redox reactions, Selenium, Silica, Magnetite, Iron, Silicon, Oxides, Nanoparticles, Polymerization, X-ray absorption near edge spectroscopy.

ABSTRACT. The reactivity of iron (II/III) oxide surfaces may be influenced by their interaction with silica, which is ubiquitous in aquatic systems. Understanding the structure-reactivity relationships of Si-coated mineral surfaces is necessary to describe the complex surface behavior of nanoscale iron oxides. Here we use Si-adsorption isotherms and FTIR spectroscopy to analyze the sorption and polymerization of silica on slightly oxidized magnetite nanoparticles (15% maghemite and 85% magnetite, i.e. ~2 maghemite surface layers), showing that Si adsorption follows a Langmuir isotherm up to 2 mM dissolved Si, where surface polymerization occurs. Furthermore, the effects of silica surface coatings on the redox-catalytic ability of magnetite are analyzed using selenium as molecular probe. The results show that for partially oxidized

nanoparticles, and even under different Si surface coverages, electron transfer is still occurring. The results indicate anion exchange between silicate and the sorbed Se^{IV} and Se^{VI}. X-ray absorption near edge structure analyses of the reacted Se indicate the formation of a mixed selenite / Se^0 surface phase. We conclude that neither partial oxidation nor silica surface coatings block the sorption and redox-catalytic properties of magnetite nanoparticles, a result with important implications to assess the reactivity of mixed-valence phases in environmental settings.

1. INTRODUCTION.

The widespread abundance of silica in natural waters, with concentrations from 1 to 30 ppm,[1] and its affinity for mineral phases make the study of mineral-silica-water interfaces particularly relevant. Silica surface coatings can modify the mineral surface reactivity, prevent further weathering of the underlying mineral[2,3] (e.g., limiting fluid transport), be involved in sorption and redox reactions, and promote the sequestration of contaminants playing therefore an important role in the mobility of contaminants in the environment.[4] Furthermore, the redox reactivity of a mineral species may be affected by the formation of silicate-rich insulating surface coatings at the mineral-water interface, impacting the quantification of the total reduction capacity (TRC) of surficial environments.[5,6]

Silica, present in solution in the form of silicate monomers at low concentrations below pH 11.5,[7] exhibits a strong affinity towards iron (hydr)oxide surfaces affecting the adsorption and mobility of cations,[8] as well as anionic species such as arsenite,[9–11] selenite,[12] and chromate.[13] Studies dealing with silicate adsorption on iron oxides are scarce, possibly because its polymerization precludes mechanistic interpretation of the interaction with mineral surfaces.[14–20] Some of these studies showed that silicate monomers form inner-sphere complexes by exchanging ligands with iron oxide surface groups forming mono- or bi-dentate surface complexes that can also exist

simultaneously at low magnetite surface loading.[7,14–16,21,22] Polymerization is shown to occur mostly at high Si surface loadings.[7,19,23]

Magnetic iron oxide nanoparticles (mostly magnetite Fe_3O_4), are promising for industrial-scale wastewater treatment, due to their low cost, strong adsorption capacity, enhanced stability and easy magnetic separation.[24] In aquatic systems, the sorption and redox properties of magnetite nanoparticles (MNPs) are influenced by the formation of a surface silica coating. Furthermore, as a mixed Fe^{II}/Fe^{III} oxide, magnetite is often non-stoichiometric (partially oxidized), an important factor to consider when evaluating its reactivity,[18,25–28] especially since electron transfer may occur only through non-oxidized mineral layers.[29] In this context, selenium represents an ideal probe to evaluate electron transfer because iron oxides are effective scavengers of selenite (SeO_3^{2-}, Se^{IV}) and selenate (SeO_4^{2-}, Se^{VI}) via adsorption processes[30–35] and reductive precipitation.[36–39] In the latter, iron oxides containing Fe^{II}, like magnetite, catalyze the reduction of Se oxyanions to produce non-soluble Se^0 and Fe selenides. The redox reactivity of MNPs towards Se oxyanions (mainly Se^{IV}) makes Se an ideal molecular probe to study the influence of silica surface coatings on sorption and redox processes.

While similar behavior has been observed between experiments in which Si and Se ions were added simultaneously and experiments in which Si and Se ions were added sequentially (magnetite shortly pre-equilibrated with Si for 3 days),[40] longer pre-equilibration times with dissolved silicates favor oligomeric and polymeric Si surfaces structures which may influence the sorption properties of iron oxides.[41] The aim of this work is to probe silicate surface chemistry and structure on MNPs and assess the effects of silica coatings on the adsorption and reduction behavior of magnetite. To this end, we have used silica-coated MNPs (Si-MNPs) for Se sorption experiments. This approach allows the precise characterization of the silica coating using Si-adsorption isotherms and infrared

spectroscopy prior to the adsorption and reduction of Se ions; described by Se^{IV} / Se^{VI} sorption kinetic experiments and X-ray absorption spectroscopy (XAS).

2. MATERIALS AND METHODS.

All solutions were prepared from analytical-grade chemicals (Sigma-Aldrich) and boiled and argon-degassed Milli-Q water.

2.1. Solid phase.

Magnetite nanoparticles (MNPs) were prepared following the method reported by Sugimoto.[42] Briefly, 8 mL of a $FeSO_4$ solution were mixed with 1 mL of 0.5 M KOH and 1 mL of 2 M KNO_3 at 90 °C under inert atmosphere for several hours until precipitation of MNPs.

Specific surface area (SSA) was determined with a multipoint N_2−BET (Brunauer−Emmett−Teller) method using a Belsorp-Max (Bel Japan) volumetric gas sorption instrument. A sample of 0.3522 g of MNPs was initially outgassed at 80 °C for 12 h under vacuum. SSA was estimated from the BET equation in the $0.05 \leq P/P0 \leq 0.26$ interval of relative pressure and using 16.2 $Å^2$ or cross-sectional area of molecular N_2.

Fourier transform infrared (FTIR) spectra of KBr pellets with MNPs at 0.3% w/w were recorded using a Thermo Fisher Scientific® Nicolet iS550 FTIR spectrometer in the range of 4000 to 400 cm^{-1} with a 4 cm^{-1} resolution, by averaging 64 scans. Specific vibrational bands were fitted using the FityK program.[43]

Raman spectrum of 30mg/mL MNPs suspension was recorded using a RXN1 instrument from Kaiser Optical operating with a 785 nm laser probe with an exposure time of 3 s and averaged over three scans.

X-ray diffraction pattern was recorded at RT using a Bruker® D8 Discover diffractometer with Cu Kα radiation (wavelength =1.54 Å) in a continuous-scan mode in the 5-80° 2θ range with a

step of 0.026°. Rietveld analysis was performed using Profex.[44] The sample was measured under Ar atmosphere in an airtight specimen holder ring with dome cap transparent to X-rays.

^{57}Fe Mössbauer spectra were recorded at 300 and 77 K using a constant acceleration transmission setup and a ^{57}Co γ-ray source diffused into a Rh matrix. A thin layer containing ~ 5 mg/cm^2 of the powdered compound was mounted on an airtight sample holder in an Ar-filled glovebox. The hyperfine structure was modeled by a least-squares fitting procedure involving Zeeman sextets composed of Lorentzian lines using program MOSFIT[45]. The values of isomer shift are quoted to that of α-Fe at 300K and an α-Fe foil was used as standard to calibrate the spectrometer.

Acid-base titration of 1.0 g/L MNPs in KNO_3 0.1M background electrolyte was carried out under a continuous N_2 flow. HNO_3 and NaOH 0.1 M solutions (Honeywell Fluka) were used as titrants. The whole system was controlled by a Metrohm® 905 titrando instrument (experimental details and data evaluation in **Text S1**).

Tapping-mode AFM images were obtained using a Digital MFP3D, Asylum Research, Oxford Instruments. Samples were prepared by dropping 50 μL of a 0.1 mg/mL MNPs suspension in ethanol on a glass slide and drying at room temperature. Data was collected at 1 Hz scan rate and 256 points per line. Surface roughness was evaluated after flattening the topography images and via calculation of Root Mean Square (RMS, details in **Text S2**) using the Asylum Research software, based in IGOR Pro (WaveMetrics, Lake Oswego, OR).

Scanning electron microscopy (SEM) was performed using a FEG Ultra55 with an acceleration voltage of 4 kV. The sample was prepared by depositing a small amount of MNPs powder on a double-sided sticky carbon tape fixed to the sample holder.

2.3. Adsorption experiments.

Silica-coated MNPs (Si-MNPs) were prepared using a sol–gel method based on the base-catalyzed hydrolysis of tetraethyl orthosilicate (TEOS), which relies on the well-known Stöber method.[46,47] Adsorption reactions were initiated by adding TEOS (1 to 10 mM final concertation) to a mixture of MNPs 0.1 M and NH_4OH 0.1 M in a 30% V/V ethanol/water. The final pH = 10 falls into the pH range of maximum silicate sorption (pH = 8-10).[22] The reaction mixture was mechanically stirred during 16 h and the Si content of the supernatant was analyzed by Inductively Coupled Plasma Optical Emission Spectrometry (ICP-OES) with a Varian 720-ES apparatus. Powders were washed four times with deionized water by magnetization and dried at 100 ºC. Then, 50 mg were digested in 1.5 mL acid (concentrated HCl, 1mL; HNO_3, 0.5 mL; and HF, 5 µL) at 60 ºC for 2 h. Following digestion, boric acid was added (2 mL, 25 g/L) to neutralize excess HF and complex fluoride, and the volume completed up to 50 mL with water prior to ICP-OES analysis.

Selenite (SeO_3^{2-}, Se^{IV}) and selenate (SeO_4^{2-}, Se^{VI}) sorption kinetics were investigated at 25 °C in an Ar-filled glovebox. Concentration of MNPs or Si-MNPs was fixed at ~5 g/L in 100 mL of NaCl 50 mM in 125 mL polypropylene tubes. The pH was adjusted to ~5 by adding HCl because the sorption of selenium anions on Fe oxides is maximized in the acid region due to the formation of positive protonated surface sites.[38,40] Suspensions were equilibrated overnight prior to the addition of aliquots of the Se stock solutions to obtain an initial concentration of Se ~1.5 mM (see **Table S3** for details). After the addition of Se^{IV} the pH dropped to ~8 and it was readjusted to pH ~5 by adding HCl. After the addition of Se^{VI} the pH remained ~5. No additional pH adjustments were done during the kinetic experiments. During the reaction, the reactors were placed in a rotary shaker. At each defined time interval, a 4 mL aliquot of the suspension was sampled by filtration through a 0.22 µm pore size membrane filter. The total concentration of Se and Si (and Fe) in the

filtrates was measured by ICP-OES after dilution with degassed ultrapure water. The difference to the initial selenium content provided the amount of sorbed Se. The Se sorption efficiency percentage was calculated using: % Se sorption = $\{([Se]_{initial} - [Se]_{final})/[Se]_{initial}\}$ x 100. Control experiments were performed under the same conditions in the absence of Se.

2.4. X-Ray Absorption Spectroscopy (XAS) measurements.

At the end of the Se sorption kinetic experiments (reaction time ≈ 1000 h, except for Si-MNPs + Se^{VI} where reaction time = 804 h), the solid products were separated by filtration, washed with water and dried at 25 °C in an Ar-filled glovebox. Bulk Se K-edge X-ray absorption near edge structure (XANES) spectra were collected at BL22-CLÆSS beamline[48] at the ALBA CELLS Spanish synchrotron. (See **Text S3** for details).

3. RESULTS AND DISCUSSION.

3.1. Magnetite characterization and surface properties.

Magnetite (Fe_3O_4) stoichiometry can be written as $Y[XY]O_4$ where $X = Fe^{2+}$, $Y = Fe^{3+}$ and the brackets denote octahedral sites (Oct). The structure consists of Oct and mixed tetrahedral (Tet)/Oct layers stacked along the [111] direction.[49] Magnetite is often non-stoichiometric, it can have a range of oxidation states dependent upon the amount of structural Fe^{2+}. For this reason, a magnetite stoichiometry parameter ($x = Fe^{2+}/Fe^{3+}$) is defined, the end members being pure magnetite ($x = 0.5$) and maghemite ($x = 0$; γ-Fe_2O_3).[50] Maghemite has a structure similar to that of magnetite, but all Fe are in the trivalent state and cation vacancies compensate for the oxidation of Fe^{2+}.

3.1.1. Identification of synthetic mineral composition. The XRD pattern of MNPs (specific surface area 22.3 m^2/g) (**Fig. S1)** shows a pure magnetite phase. However, XRD patterns of

maghemite and magnetite are very similar, with slight shifts in the peak positions due to their different unit cell lenghts.[51] The reported unit cell parameter for stoichiometric magnetite is a = 8.40 Å. As magnetite becomes non-stoichiometric, the unit cell becomes smaller due to the formation of vacancies and the smaller atomic size of Fe^{3+} atoms as compared to Fe^{2+} (a = 8.34 Å for maghemite).[49,50] The unit cell length for MNPs calculated by Rietveld analysis is a = 8.394 Å, indicating a non-stoichiometric magnetite. The Raman spectrum of MNPs (**Fig. S2**) is well consistent with those reported on magnetite, showing a pronounced peak at ~670 cm^{-1}, and weak peaks at 310 and 534 cm^{-1}.[52] The FTIR spectrum of MNPs (**Fig. S3**) shows a strong and broad band at 584 cm^{-1}, assigned to the Fe−O stretching mode of the tetrahedral and octahedral sites of magnetite, and additional shoulders at 628 and 705 cm^{-1} due to magnetite non-stoichiometry.[51]

3.1.2. Stoichiometry. Both XRD and FTIR indicate that MNPs are non-stoichiometric. However, although these techniques have been used to distinguish between magnetite and maghemite,[50,51,53] accurate stoichiometry quantification remains difficult using optical spectroscopy techniques. Mössbauer spectroscopy, on the other hand, is a powerful tool for the identification of charge and coordination of iron species.[54] As shown in **Fig. S4**, the room temperature Mössbauer spectrum of MNPs which is composed of two magnetic sextets, is rather similar to that of magnetite but the intensities of these two components differ from expected ones, corresponding to $^{Oct,Tet}Fe^{3+}$ and $^{Oct}Fe^{2.5+}$. A first description consists in two independent magnetic components (**Fig. S4a**) and the corresponding refined values of hyperfine parameters are listed in **Table S1**. This decomposition allows then to estimate the proportions of magnetite and maghemite from the mean value of the isomer shift by interpolation from those of stoichiometric magnetite and maghemite.[55] A second fitting model (**Fig. S4b**) consists in combining 4 magnetic components: two typical of ideal magnetite and the two others typical of ideal maghemite (with

theoretical absorption areas ratio of 0.5 and 0.6, respectively). The analysis of the spectrum gives 85% stoichiometric magnetite and 15% stoichiometric maghemite. Therefore, the stoichiometry of MNPs was calculated as $x = 0.425$. It is important to note that the study performed at 77K (spectrum not shown here) confirms perfectly that at 300K. Assuming a preferential oxidation at the surface of the MNPs, the result leads to a maghemite layer thickness of approximately 1.47 nm corresponding to about 2 maghemite layers and suggesting that the surface of MNPs is covered by maghemite. Nevertheless, with our experimental data it is not possible to determine whether the oxidation occurs at the surface or in the bulk of the particles (solid solution).

3.1.3. Morphology and Surface Properties. The morphology of MNPs was characterized by scanning electron microscopic (SEM) (**Fig. S5)**. The particles are octahedral crystals bounded by [111] plane with an approximate crystal size of ~80 nm. AFM imaging and crystallite roughness analysis (**Fig. S6)** indicate a mean square roughness (RMS) of 2 nm, in the same order of magnitude as the 3.2 nm reported values for 5µm size iron oxide particles.[56] Ligand exchange involving hydroxyl surface sites is one of the main mechanisms of adsorption at the magnetite-water interface. The surface site density (D_s) of MNPs was determined via acid-base titration following two different data evaluation protocols (see **Text S1**). D_s values for MNPs were between 2.90 and 3.08 sites/nm^2, which is within the range of values reported in the literature (~1-2 sites/nm^2 [8,9,12] to ~5 sites/nm^2 [61–63]) and is in the same order of magnitude of the theoretical crystallographic value of 8 sites/nm^2, obtained using crystal-chemistry considerations and crystallographic data of the [111] plane of magnetite.[64]

3.2. Si sorption.

3.2.1. Si adsorption isotherm. To acquire a better understanding of the mechanisms involved in the adsorption of Si onto MNPs surfaces during the formation of the silica-coated MNPS (Si-

MNPS), we constructed an adsorption isotherm (**Fig. 1**) by measuring the extent to which MNPs remove Si from the reaction solution (pH 10). Three different regimes are proposed: *(i) Adsorption/oligomerization regime*: at dissolved Si concentrations, $[Si]_{aq}$, below 2 x 10^{-3} M, Si sorption, $[Si]_{sorbed}$, increases with increasing $[Si]_{aq}$. The experimental data in this concentration range can be fitted with a Langmuir isotherm:

$$\tau_{Si} = \tau_{ads} \times \frac{k_{ads}[Si]_{aq}}{1 + k_{ads}[Si]_{aq}}$$

where τ_{Si} is the Si surface loading, τ_{ads} is the total site density, and K_{ads} is the Langmuir constant. The maximum adsorption capacity (τ_{ads}) obtained for MNPs is 8.3 sites/nm^2, in agreement with the estimated crystallographic D_s (8 sites/nm^2) but slightly higher than the D_s values determined via acid-base titrations (see section 3.1.3 above). Nevertheless, FTIR analysis (see section 3.2.2 below) indicate that in this regime the only surface Si species formed are monomers and oligomers. *(ii) Polymerization/precipitation regime*: a surface precipitation event occurs when $[Si]_{sorbed}$ increases dramatically at $[Si]_{aq} \approx 2 \times 10^{-3}$ M, which matches well the equilibrium constant for the solubility of amorphous silica in water (K^o_{eq} ($aSiO_2$) = 2 x 10^{-3} at 25ºC and 1 atm).[65] This transition from adsorption/oligomerization to surface precipitation was also observed for silicate on hematite[66] and can be ascribed by Si surface polymerization.[7] However, sorbed Si may also represent sorption of polymers from solution since the presence of dissolved Si polymers is favored at high $[Si]_{aq}$.[7] On the basis of our results only, it is not possible to evaluate the quantitative contribution of either process to the pronounced increase of Si sorption at $[Si]_{aq} \approx 2 \times 10^{-3}$ M. *(iii) Homogeneous precipitation* regime: at dissolved Si concentrations exceeding K^o_{eq} ($aSiO_2$), $[Si]_{sorbed}$ remains constant with increasing $[Si]_{aq}$. This behavior can be attributed to Si precipitation in solution due to the formation of small clusters, oligomers and polymers at high $[Si]_{aq}$ regardless of the pH.[7]

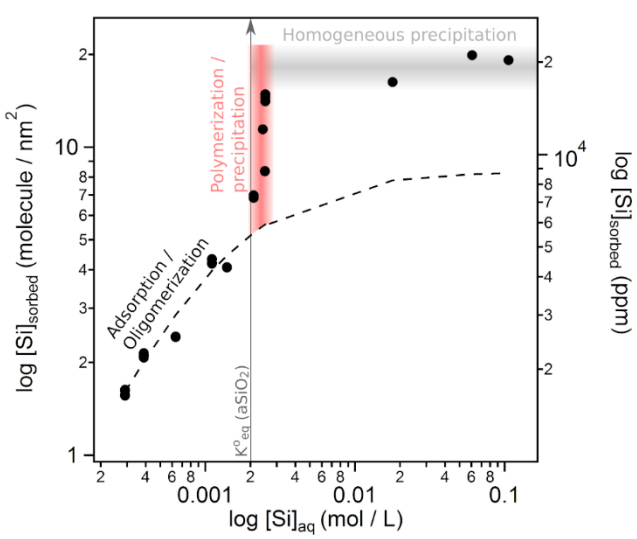

233

234 **Figure 1**. Si adsorption isotherm for MNPs after 16 h equilibration at pH = 10. Dotted lines
235 correspond to the best-fit data by using a Langmuir isotherm. The arrow indicates the solubility of
236 amorphous silica in water (K^{o}_{eq} (aSiO$_2$)), at this point surface polymerization / precipitation at the
237 surface of MNPs (red colored area) followed by homogeneous precipitation in solution (grey
238 colored area) occur.

239

240 **3.2.2. Surface Si species.** To investigate the speciation of sorbed Si on the surface of MNPs at
241 the different regimes related to the Si-adsorption isotherm, we characterized a series of Si-MNPs
242 with increasing Si content using FTIR, which has been successfully used to study the degree of
243 polymerization of silicates via the analysis of the different Si-O vibrations bands.[7,19,23]. **Fig. 2a**
244 shows the FTIR spectra of Si-MNPs with different Si contents in the region between 1300 and 850
245 cm^{-1}, characteristic for IR bands of sorbed silicate.[67–69] IR absorbance bands in this range are only
246 detected at [Si]$_{sorbed}$ ≥ 4000ppm, below this concentration the spectra is similar to that of bare
247 MNPs. In order to distinguish the spectral features of the various Si-MNPs we performed curve
248 fitting of the absorption bands (see **Fig. S9** for deconvoluted spectra). The number of component
249 bands, band areas, and peak maxima locations vary with [Si]$_{sorbed}$ (**Table S2, Fig. S10a**).

Moreover, using the integrated area of each fitted absorption band we obtained quantitative information about each silicate species in terms of percentage (**Fig. 2b**) and absolute content (**Fig. S10b**).

Adsorption/oligomerization regime: At $[Si]_{sorbed}$ between 4000 and 4700 ppm, IR absorbance appears between 850 and 1100 cm^{-1} (**Fig. 2a**). An absorbance maximum was determined at ~990 cm^{-1}, together with less intense bands at ~890, ~925 and ~1040 cm^{-1} (**Table S2, Fig. S10a**). Previous studies attributed the different peaks in this region of the spectra to monomeric, oligomeric, and polymeric Si surface configurations, which can be distinguished based on the position of the Si−O stretching bands.[7,19,23] The IR bands between 890 and 950 cm^{-1} are attributed to monomeric species.[7] The maximum IR absorption of the oligomer occurs at ~1000 cm^{-1}, while a shift to 1050 cm^{-1} indicates oligomeric species with a higher degree of polymerization.[19] Based on the described band assignments, at $[Si]_{sorbed}$ = 4000 - 4700 ppm, silicate forms exclusively monomeric and oligomeric species, accounting for ~30 and ~70 % of the area of the spectrum respectively (**Fig. 2b**).

Polymerization/precipitation regime: At $[Si]_{sorbed}$ between 6300 and 12000 ppm, all resolved bands of sorbed silicate shifted to higher frequency with increasing surface coverage (**Fig. 2a**), reaching an absorbance maximum at 1061 cm^{-1} for $[Si]_{sorbed}$ = 12000 ppm (**Table S2, Fig. S10a**). Moreover, new bands appeared at >1100cm^{-1}. Generally, the band positions of stretching vibrations of Si surface species are shifted to higher wavenumbers with increasing degree of condensation. IR absorbance in the wavenumber region 1050-1200 cm^{-1} is related to polymeric species, and bands at wavenumbers > 1100 cm^{-1} have been assigned to a 3D framework such as amorphous silica.[7,19,23] **Fig. 2b** shows that during the surface precipitation regime, the percentage of polymeric species increase from 10 to 86% of the area of the spectrum, while monomeric species

decrease from 30 to 14%. Interestingly, oligomeric species decrease from 60 to 0%, indicating that all oligomers condense to form high polymers.

Homogeneous precipitation regime: At $[Si]_{sorbed}$ >17500 ppm, all resolved bands remain essentially at the same position (**Table S2, Fig. S10a**) and the percentage of each silicate species remains constant (**Fig. 2b**), which agrees with the homogeneous precipitation regime of the Si-isotherm.

It is important to highlight that the absolute content of Si-monomers remains constant for all the range of $[Si]_{sorbed}$ (**Fig. S10b**), suggesting that a minimum of ~2000 ppm of Si, corresponding to adsorbed monomers, is required prior to the occurrence of polymerization. Notably, this value corresponds to ~2.14 sites/nm^2, which is similar to the D_s of MNPs calculated by acid-base titrations (2.90 - 3.08 sites/nm^2, see above). Accordingly, the relationship between the number of sites occupied by Si monomers and D_s highlights the vital role of active site density in Si adsorption and polymerization on MNPs.

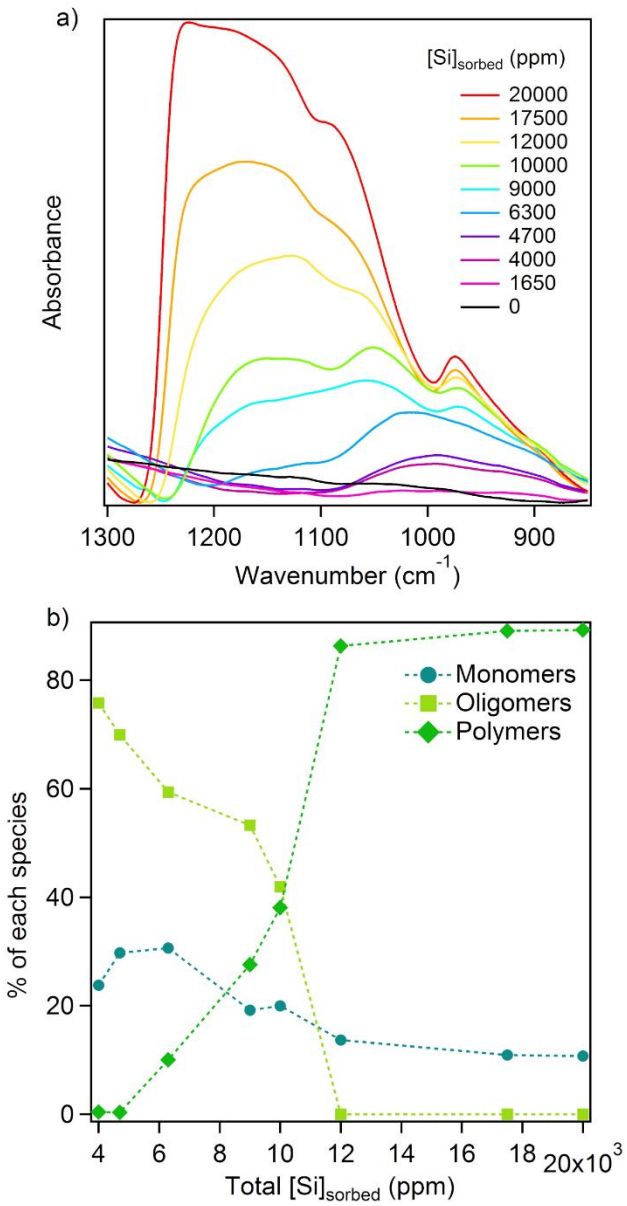

286

287 **Figure 2**. a) FTIR spectra of Si-MNPs with different Si content. Baseline correction, smoothing
288 and normalization to the maximum intensity of the highest peak (584 cm^{-1} magnetite's Fe–O
289 stretching mode) was performed using SpectraGryph software. b) Percentage of each Si-species
290 calculated using the integrated areas of fitted absorption bands.

291 **3.3. Effect of silica coating on Se sorption.**

3.3.1. Se sorption kinetics. To study the influence of silica coatings on the sorption of Se^{IV} and Se^{VI} by MNPs, we utilized Si-MNPs with different Si content: *(1)* $[Si]_{sorbed}$ = 4000 ppm, that fall in the adsorption/oligomerization regime of the Si-adsorption isotherm and are composed of 24% monomers and 76% oligomers (abbreviated thereafter as Si_{ads}-MNPs); and *(2)* $[Si]_{sorbed}$ = 10000 ppm, that fall in the polymerization/precipitation regime and contain 20, 42 and 38% of monomers, oligomers and polymers respectively (Si_{pol}-MNPs).

Se^{IV} sorption: The results of Se^{IV} kinetic sorption experiments at pH ≈ 5 are shown in **Fig. 3a** and **Table S3**. In the absence of Si, the concentration of Se sorbed, $[Se]_{sorbed}$, increased rapidly within the first hour to ~2 Se/nm^2, and then raised slightly to reach 2.5 Se/nm^2, corresponding to 30% of Se sorption efficiency. This relatively low sorption percentage can be attributed to the saturation of sorption sites of adsorbent in the presence of high concentrations of adsorbate.[70] The initial Se^{IV} concentration, $[Se^{IV}]_{aq}$, was chosen according to the concentration of reactive sites [–Fe–OH] based on the estimated crystallographic D_s (8 sites/nm^2). However, D_s of MNPs calculated by acid-base titrations was smaller (2.90-3.08 sites/nm^2, see above), which may explain the decrease in Se^{IV} sorption efficiency.

In the case of Si-MNPs, the Se^{IV} uptake performance decreases compared to bare MNPs and the sorption kinetics are slower as the Si coverage increases (**Fig. 3a** and **Table S3).** Although the kinetics were different, final $[Se]_{sorbed}$ and sorption efficiency were the same for both, Si_{ads}-MNPs and Si_{pol}-MNPs. Examining Si desorption from Si-MNPs during Se^{IV} sorption experiments explains why the sorption of selenite was slower in the presence of Si coatings. **Fig. 3b** shows that Si is slowly desorbed from magnetite during the first ~300h, probably due to the lower affinity of Si for the magnetite surface at pH < 8.[22] Moreover, Si desorption kinetics are slower as the Si coverage increases due to the presence of more extended polymeric surface silicate species. For

both Si-MNPs samples, the final Si sorbed decreased to a value of ~750 ppm, which corresponds to ~0.7 Si/nm^2 (**Fig. 3b** and **Table S3**). This final concentration of silicate probably corresponds to firmly bonded monomeric species, forming covalently bonded inner-sphere complexes.[7] However, in the absence of selenium Si is desorbed to a lesser extent under the same conditions; reaching final Si sorbed values of 2.2 Si/nm^2 for Si_{ads}-MNPs and 3.3 Si/nm^2 for Si_{pol}-MNPs (**Fig. 3b**). Noteworthy, the final total site densities occupied by Si + Se were 2.2 and 2.4 sites/nm^2 for Si_{ads}-MNPs and Si_{pol}-MNPs respectively, which are in the range of *i)* the $[Se]_{sorbed}$ in the absence of Si; *ii)* the final Si sorbed in the absence of Se^{IV}; and *iii)* the D_s of MNPs calculated by acid-base titrations (2.90-3.08 sites/nm^2, see above). The effect of Si on the Se^{IV} sorption efficiency can then be attributed to a competition between both anions for the surface sites. Reported ion-competitive studies showed that when silicate was present in the solution, the sorption of selenite onto magnetite decreased due to changes in surface charge potential and magnetite surface site availability upon adsorption of silicate species.[12,40] The silicate monomeric/oligomeric species present in Si_{ads}-MNPs modify the surface charge potential of magnetite (point zero charge, pH_{pzc}, ≈ 7 for magnetite[71,72] and ≈ 3 for silica[73]) as well as the surface sites availability. On the other hand, the high percentage of polymers present on the surface of Si_{pol}-MNPs does not seem to prevent Se^{IV} adsorption, only a decrease in the kinetics of adsorption is observed. Summarizing: *1)* Desorption of already sorbed silica on the magnetite surface gradually freed up new sorption sites and, thus, selenite and silicate compete for those sites; therefore, *2)* Se^{IV} sorption kinetics are influenced by Si-desorption kinetics. Finally, *3)* Si coatings affect Se^{IV} sorption efficiency since ~0.7 sites/nm^2 remained occupied by surface silicate monomeric species firmly attached to the magnetite surface, hindering the sorption of selenite onto magnetite – this may also suggest a site-specific silicate sorption onto magnetite's surface.

Se^{VI} sorption: **Fig. 3c** and **Table S3** show the results of Se^{VI} kinetic sorption experiments under the same conditions as for Se^{IV}. Both, MNPs and Si-MNPs show the same Se^{VI} sorption efficiency and kinetics, which are independent of silicate coverage. After 300h, the final $[Se]_{sorbed}$ is ~1 Se/nm^2 for all samples and Se sorption efficiencies were between 10 and 14%. Compared with Se^{IV}, Se^{VI} sorption kinetics are slower and less efficient, especially for bare MNPs, since Se^{VI} has a lower affinity for Fe-bearing minerals and it reacts with much slower kinetics than Se^{IV}.[33,40,74,75] The slow Se^{VI} sorption kinetics were also reflected in the measured amounts of desorbed Si: In the presence of Se^{VI}, the Si desorption kinetics (**Fig. 3d)** are slower compared to Se^{IV}. Moreover, less Si is removed during Se^{VI} sorption experiments, since the final $[Si]_{sorbed}$ is ~1.5 Si/nm^2, whereas Se^{IV} experiments resulted in a final $[Si]_{sorbed}$ of ~0.7 Si/nm^2 (**Table S3**). Note that, additionally, the difference in the final $[Si]_{sorbed}$ in the absence / presence of Se^{VI} is less pronounced than the final $[Si]_{sorbed}$ in the absence / presence of Se^{IV} (**Fig. 3d**). This behavior can be explained by the slower Se^{VI} sorption compared with Si desorption kinetics on magnetite (**Fig. 3c, d**); during Si desorption there is virtually no competition with Se adsorption, and therefore, even at pH 5 some desorbed silicate can be re-adsorbed. Although the maximal percentage of silicate adsorption is located between pH 8 and 10, silicate can bind on the surface of magnetite over a wider pH range in the absence of competing species.[22] Note that for silicate concentrations under the solubility limit of amorphous silica (2 x 10^{-3} M), as in our experiments (**Table S3**), only monomeric species are present in solution from pH 4 to 10.[76] Importantly, the total site density occupied by Si + Se is similar for Se^{IV} and Se^{VI} experiments (2.2 - 2.9 sites/nm^2) and agrees with the total coverage of surface reactive sites. Nevertheless, in the absence of silicate competing ions, Se^{VI} sorption only reached ~1 site/nm^2, confirming the lower reactivity of Se^{VI} vs. Se^{IV}. Recapitulating: *1)* Se^{VI} sorption is less efficient and slower than Se^{IV} sorption. *2)* The slow kinetics of Se^{VI} sorption onto

magnetite makes this reaction independent of Si coverage since there is time enough to free up sorption sites due to Si desorption (effectively no competition with silicate); which, in turn, 3) results in lower Si-desorption (higher final $[Si]_{sorbed}$) compared with the reaction that starts with Se^{IV}.

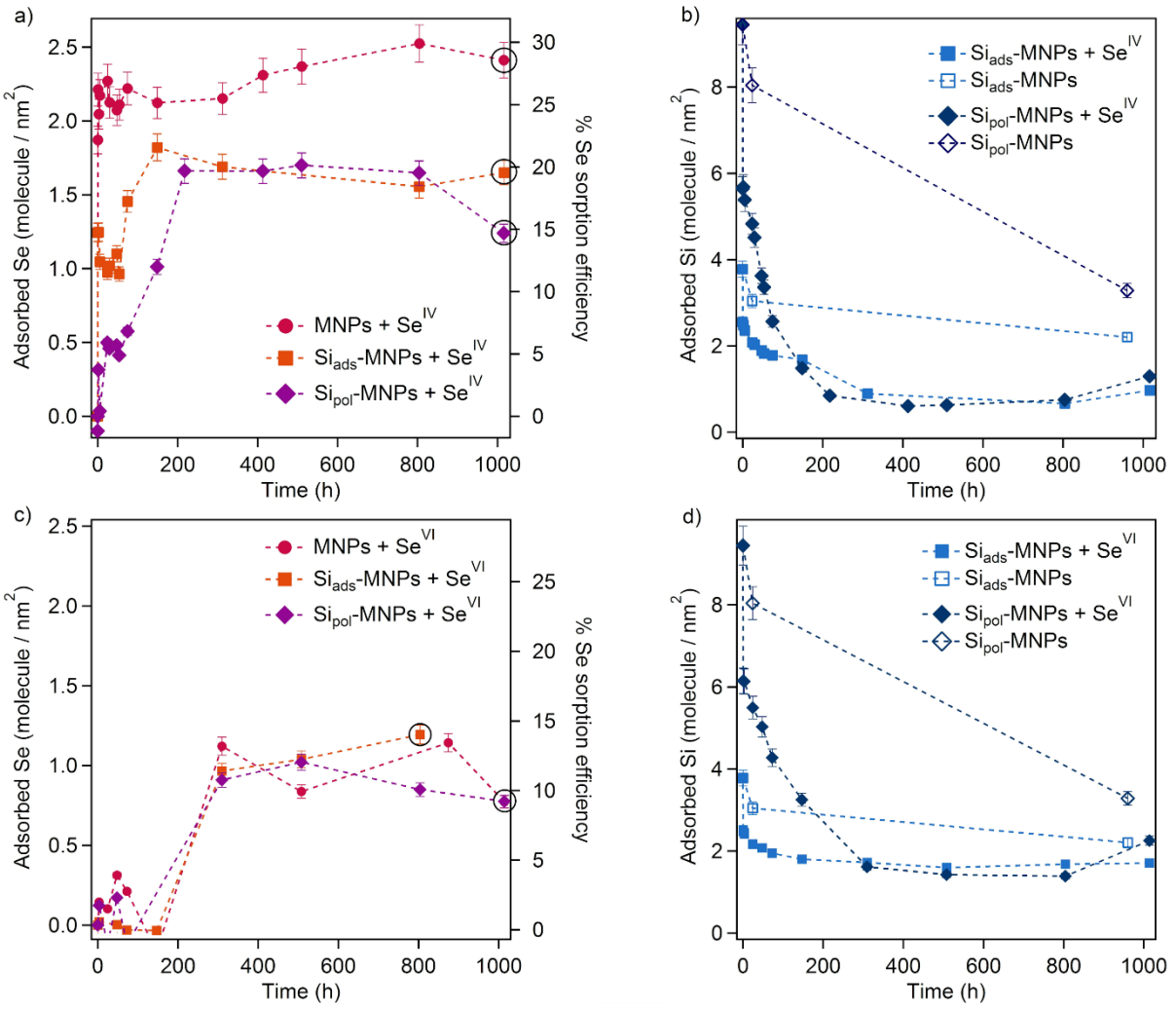

Fig 3. a) Sorption kinetics of Se^{IV}, b) Desorption kinetics of Si in the absence/presence of Se^{IV}, c) Sorption kinetics of Se^{VI}, and d) Desorption kinetics of Si in the absence/presence of Se^{VI}. The black circles denote the samples used for XANES measurements (see below). Initial Si content in the desorption graphs (at t = 0 h) corresponds to the Si sorbed prior to the pre-equilibration step.

Error bars correspond to a 5% estimate ICP-OES error, determined from repeated analysis of standards.

3.3.2. Surface Se species. Sorption products at the end of the kinetics experiments (reaction time ≈ 1000 h, except for Si_{ads}-MNPs + Se^{VI} where reaction time = 804 h) were characterized by Se K-edge XANES.

Se^{IV} sorption: Linear combination fits (LCF) analysis of the Se K-edge XANES spectra of the solid residues from the experiments with Se^{IV} revealed the presence of Se^{IV} and Se^0 (**Fig. 4, Table S4**). Clearly, as Se^{IV} is adsorbed, it is reduced to elemental Se^0 using the electrons generated from the oxidation of Fe^{2+} in magnetite; note that reduction by aqueous Fe^{2+} dissolved from magnetite can be ruled out (see **Table S5**). This result suggests that magnetite can immobilize Se^{IV} through two different mechanisms: surface adsorption and reductive precipitation. In reductive precipitation processes, Fe^{II}-bearing minerals catalyze the reduction of Se^{IV} forming predominantly Se^0, but also Fe selenides (FeSe, and $FeSe_2$) depending on the experimental conditions.[36,37,39,77,78] In adsorption processes, sorbed Se^{IV} may form inner-sphere ($FeSeO_3$) and outer-sphere (Na_2SeO_3 electrostatic sorption) complexes.[77,79–81] Although Se^{IV} is generally sorbed by bidentate inner-sphere complexation,[78] the exact Se^{IV} solid species in our system are hard to describe by our XANES measurements. For MNPs, LCF analysis resulted in 24% of Se^0 reduced species and 76% of Se^{IV} unreduced surface complexes (**Table S4, Fig. 4b**). It is important to note that, although Mössbauer data (see **section 3.1.2**) indicated that MNPs are slightly oxidized (15% maghemite, ~2 maghemite surface layers assuming oxidation at the surface), electron transfer is still occurring. However, in the presence of Si, the percentage of Se^0 in the solid products was smaller and decreased as the initial Si coverage increased (**Table S4, Fig. 4b**); indicating that not only Si hinders the electron transfer between magnetite and Se^{IV}, but also the competition between

selenite and silicate for the surface sites observed in the kinetic experiments affects the redox reactivity.

Se^{VI} sorption: The XANES spectra of the solid residues from the experiments with Se^{VI} (**Fig. 4a**) revealed the presence of Se^{IV} and Se^0, indicating that either all Se^{VI} was reduced to Se^{IV} and Se^0; or that adsorbed Se^{VI} is washed away from solids during the filtration and washing procedures (Se^{VI} is generally presumed to form outer-sphere complexes[82]). Similarly, Onoguchi *et al.*[37] recently reported the reduction of selenate into selenite and elemental Se^0 catalyzed by green rusts (GR) through two different mechanisms: *i)* after adsorption (homogeneous redox reaction); and *ii)* without adsorption (heterogeneous redox reaction), where dissolved Se^{VI} could be reduced upon contact with GR. Our attempts to detect Se^{IV} in solution by ionic chromatography (IC) analysis were not successful, except in one sample; the filtrate fraction from the MNPs + Se^{VI} experiment after ~1000 h revealed that ~2 % of total selenium was Se^{IV} (data not shown). Clearly, at pH 5, Se^{IV} is strongly sorbed on the positively charged magnetite surface, and indeed constitutes the dominant solid phase selenium species. LCF analysis results (**Table S4, Fig. 4b**) indicated that the relative proportion of total Se present as Se^0 was lower when the reaction starts with Se^{VI} than when the reaction starts with Se^{IV}, indicating that the reduction of selenate to selenite influences the overall kinetics of selenium reduction. Furthermore, when Si_{ads}-MNPs was used as adsorbent, the percentage of Se^0 in the solid product not only was lower than in the absence of Si, as expected; but also lower than when the reaction starts with Se^{IV} for the same Si_{ads}-MNPs adsorbent. This is a consequence from the sum of two effects: *i)* the Se^{VI} to Se^{IV} reaction influencing the overall kinetics of Se reduction; and *ii)* the higher final $[Si]_{sorbed}$ on the surface of magnetite (1.5 vs. 0.7 Si/nm^2 for the reaction starting with selenate and selenite respectively, see **section 3.3.1** above) hindering electron transfer.

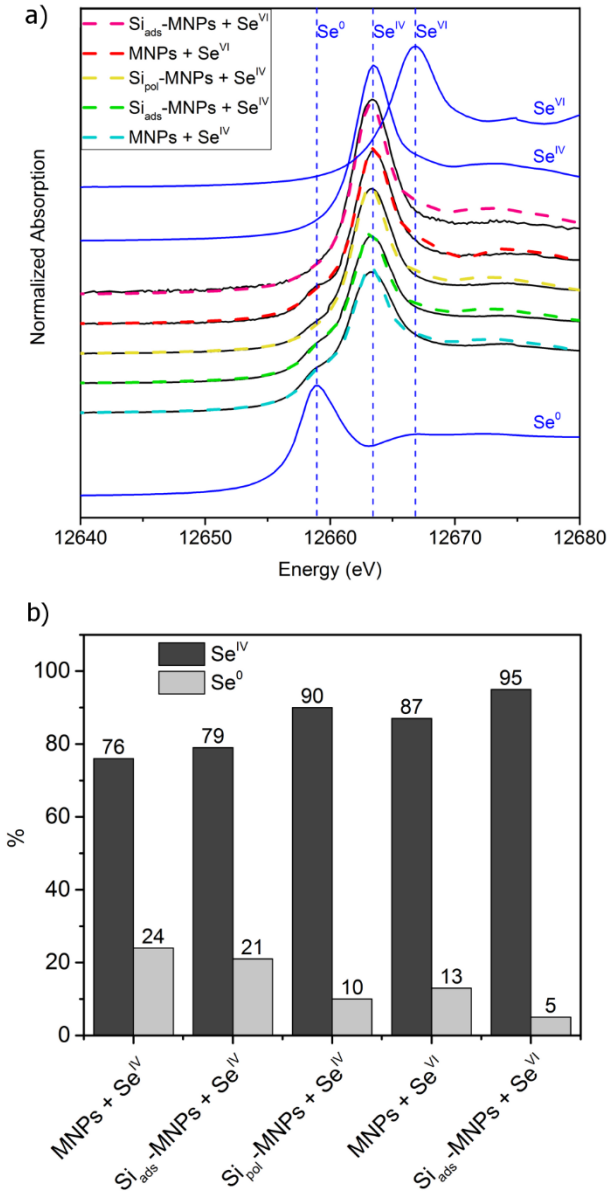

Figure 4. **a)** Se K-edge normalized XANES spectra with LCF results and related Se references and **b)** Percentage of Se components normalized to a sum of 100% for Se^{IV} and Se^{VI} sorption products at the end of the kinetic experiments (reaction time ≈ 1000 h, except for Si_{ads}-MNPs + Se^{VI} where reaction time = 804 h).

3.3.3. Kinetics pathways of Se reduction in the presence of silica coatings.

Se^{VI} to Se^{IV}: The first limiting step is the reduction of selenate to selenite. As described above, this reaction influences the overall kinetics of Se reduction. Furthermore, the lack of competition with silicate of this reaction results in a final $[Si]_{sorbed}$ 2 times higher than when the reaction starts with Se^{IV}, hindering further electron transfer. Accordingly, when the reaction starts with selenate, the reduction to selenite results in a $[Se]_{sorbed}$ that is about half of the $[Se]_{sorbed}$ when the reaction starts directly with selenite.

Se^{IV} to Se^{0}: Reduction of selenite anions is another step limiting the reaction: as selenite is adsorbed, it is reduced by surface ferrous iron to Se^0 (s). This would imply that the stability of Se^{IV} inner-sphere surface complexes at the interface is one of the steps limiting the redox reactivity. Furthermore, the competition between selenite and silicate limits the redox reactivity with the kinetics slowed down as more silicate is initially introduced.

3.6. Environmental implications.

Magnetite contributes, together with iron(II) rich clay, sulfide and carbonate minerals, to the total reduction capacity (TRC) of surficial environments (e.g. sediment or geological formations). TRC is either measured by titration with a strong oxidant, such as permanganate or dichromate, or computed based on chemical and mineralogical analysis.[83] It has been defined as the sum of reduced species present in the system:[6]

$$TRC = 4C_{org} + 7S(-I) + 8S(-II) + 8N(-III) + 2Mn(II) + Fe(II)$$

where S(-I) is attributed to pyrite (content often derived from total S content assuming no other sulphur species), Mn(II) from the total Mn content (assuming no MnO_2) and Fe(II) from the pyrite, siderite and magnetite contents (Fe(II) in clay fraction often omitted because deemed to be less reactive). N(-I) and N(-II) are usually neglected. The way to quantify the amount of the 'active'

447 species in such TRC computations is still a topic of debate: It has been shown that electron transfer
448 may occur only along specific crystallographic axes,[84] and perhaps only through thin non-oxidized
449 layers of the minerals,[29] which would decrease the effective concentration of reactive mineral mass
450 susceptible of acting in redox reactions. These and other environmental constraints, such as the
451 presence of a silicate rich insulating surface,[5] could also affect quantification of the TRC. Here we
452 investigated using wet chemistry and spectroscopic methods the redox-catalytic reactivity of
453 slightly oxidized magnetite nanoparticles (15% maghemite and 85% magnetite, i.e. ~2 maghemite
454 surface layers) and the effect of silicate adsorption and polymerization on this reactivity. First, we
455 show that silicate ions are adsorbed, according to FTIR, as monomeric Si surface complexes and
456 short-chain oligomers, the adsorption following a Langmuir-type isotherm, up to 2 x 10^{-3} M. This
457 dissolved Si concentration happens to coincide with the amorphous silica equilibrium
458 concentration, and a typical concentration found in surface waters.[65] Above that concentration,
459 surface silicate polymers form. Both oligomeric and polymeric surface complexes are shown to be
460 displaced by selenite anions. Reduction of selenite anions to elemental Se catalyzed by the
461 nanoparticles appears to be an important step limiting the reaction; in the case of selenate, all
462 selenate is reduced to selenite before the Se^0 (s) precipitates, influencing the overall reduction
463 kinetics. All these processes seem to take place independently of the silicate coverage, with the
464 kinetics slowing down as more silicate is initially introduced. A competition between selenite and
465 silicate seems to be at place, with silicate being desorbed as selenite is adsorbed, that is limiting
466 nanomagnetite reactivity towards oxyanion contaminants. The observed reduction of selenium
467 oxyanions, used here as molecular probes, demonstrates that neither a partial oxidation nor a partial
468 coverage by silica can prevent magnetite particle to be redox reactive. Such findings were also

observed on electron transfer occurring through the basal plane silicate layer of clay minerals,[85,86] and may have important consequences in magnetite driven nanotoxicity.[87]

ASSOCIATED CONTENT

Supporting Information. Texts: Measurement and data evaluation details for potentiometric acid–base titration, AFM Root Mean Square, and XAS. Figures: XRD pattern; Raman, FTIR and Mössbauer spectra; and SEM / AFM Amplitude retrace images of synthetized MNPs. Curve fitting results of the absorption bands for Si-MNPs and the resulting peak positions / areas and absolute Si content of each species. Tables: Mössbauer parameters for MNPs at T = 300 K, band areas and peak maxima locations results from the curve fitting of the FTIR absorption bands of Si-MNPs, Se sorption conditions and results, and linear combination fit (LCF) results of the XANES data.

AUTHOR INFORMATION

Corresponding Author

*Sara Goberna-Ferrón: orcid.org/0000-0002-3306-3791; Phone: +34937373610; Email: sara.goberna@icn2.cat

*Alejandro Fernández-Martínez: orcid.org/0000-0001-5073-9629; Phone: +33(0)476635197; Email: alex.fernandez-martinez@univ-grenoble-alpes.fr

Present Addresses

†Catalan Institute of Nanoscience and Nanotechnology, ICN2 (CSIC, BIST), Campus UAB, Bellaterra, 08193, Barcelona, Spain.

Author Contributions

The manuscript was written through contributions of all authors. All authors have given approval to the final version of the manuscript.

ACKNOWLEDGMENT

ANDRA (Agence Nationale pour la gestion des Déchets Radioactifs, Châtenay-Malabry) for project funding and laboratory equipment related to this work. Maria P. Asta has received financial support from the European Commission through the Marie Skłodowska-Curie Research Fellowship Programme. The XAS measurements were carried out in CLAESS beamline at the ALBA synchrotron. Funding from a grant from Labex OSUG@2020 (Investissements d'avenir, ANR10-LABX56) is acknowledged.

REFERENCES

(1) Hem, J. D. Study and Interpretation of the Chemical Characteristics of Natural Water. *US Geol. Surv. Water-Supply Pap.* **1985**, *2254*.

(2) Hellmann, R.; Daval, D.; Wirth, R. Formation of Amorphous Silica Surface Layers by Dissolution-Reprecipitaton During Chemical Weathering: Implications for CO2 Uptake. *Procedia Earth Planet. Sci.* **2013**, *7*, 346–349.

(3) Daval, D.; Sissmann, O.; Corvisier, J.; Garcia, B.; Martinez, I.; Guyot, F.; Hellmann, R. The Effect of Silica Coatings on the Weathering Rates of Wollastonite ($CaSiO_3$) and Forsterite (Mg_2SiO_4): An Apparent Paradox? In *Water-Rock Interaction*; Birkle, P., Torres-Alvarado, I.S., Eds.; Taylor & Francis Group, London 2010; pp 713–716.

(4) Schindler, M.; Singer, D. M. Mineral Surface Coatings: Environmental Records at the Nanoscale. *Elements* **2017**, *13* (3), 159–164.

(5) Jones, A. M.; Collins, R. N.; Rose, J.; Waite, T. D. The Effect of Silica and Natural Organic Matter on the Fe(II)-Catalysed Transformation and Reactivity of Fe(III) Minerals. *Geochim. Cosmochim. Acta* **2009**, *73* (15), 4409–4422.

(6) Heron, G.; Christensen, T. H. Impact of Sediment-Bound Iron on Redox Buffering in a Landfill Leachate Polluted Aquifer (Vejen, Denmark). *Environ. Sci. Technol.* **1995**, *29* (1), 187–192.

(7) Yang, X.; Roonasi, P.; Holmgren, A. A Study of Sodium Silicate in Aqueous Solution and Sorbed by Synthetic Magnetite Using in Situ ATR-FTIR Spectroscopy. *J. Colloid Interface Sci.* **2008**, *328* (1), 41–47.

(8) Marmier, N.; Fromage, F. Sorption of Cs(I) on Magnetite in the Presence of Silicates. *J. Colloid Interface Sci.* **2000**, *223* (1), 83–88.

(9) Swedlund, P. J.; Webster, J. G. Adsorption and Polymerisation of Silicic Acid on Ferrihydrite, and Its Effect on Arsenic Adsorption. *Water Res.* **1999**, *33* (16), 3413–3422.

(10) Luxton, T. P.; Eick, M. J.; Rimstidt, D. J. The Role of Silicate in the Adsorption/Desorption of Arsenite on Goethite. *Chem. Geol.* **2008**, *252* (3–4), 125–135.

(11) Kanematsu, M.; Young, T. M.; Fukushi, K.; Green, P. G.; Darby, J. L. Individual and Combined Effects of Water Quality and Empty Bed Contact Time on As(V) Removal by a Fixed-Bed Iron Oxide Adsorber: Implication for Silicate Precoating. *Water Res.* **2012**, *46* (16), 5061–5070.

(12) Jordan, N.; Lomenech, C.; Marmier, N.; Giffaut, E.; Ehrhardt, J. J. Sorption of Selenium(IV) onto Magnetite in the Presence of Silicic Acid. *J. Colloid Interface Sci.* **2009**, *329* (1), 17–23.

(13) Garman, S. M.; Luxton, T. P.; Eick, M. J. Kinetics of Chromate Adsorption on Goethite in the Presence of Sorbed Silicic Acid. *J. Environ. Qual.* **2004**, *33* (5), 1703–1708.

(14) Eick, M. J.; Luxton, T. P.; Welsh, H. A. Effect of Silica Polymerization on the Oxalate-Promoted Dissolution of Goethite. *Clays Clay Miner.* **2009**, *57* (5), 578–585.

(15) Kanematsu, M.; Waychunas, G. A.; Boily, J.-F. Silicate Binding and Precipitation on Iron Oxyhydroxides. *Environ. Sci. Technol.* **2018**, *52* (4), 1827–1833.

(16) Hiemstra, T.; Barnett, M. O.; van Riemsdijk, W. H. Interaction of Silicic Acid with Goethite. *J. Colloid Interface Sci.* **2007**, *310* (1), 8–17.

(17) Davis, C. C.; Chen, H. W.; Edwards, M. Modeling Silica Sorption to Iron Hydroxide. *Environ. Sci. Technol.* **2002**, *36* (4), 582–587.

(18) Elgaroshi, S.; Miskelly, G. M.; Swedlund, P. J. H 4 SiO 4 Sorption and Polymerization at the Magnetite - Aqueous Interface: The Influence of Interfacial Redox State. *Appl. Geochemistry* **2019**, *104*, 146–157.

(19) Yang, X.; Roonasi, P.; Jolsterå, R.; Holmgren, A. Kinetics of Silicate Sorption on Magnetite and Maghemite: An in Situ ATR-FTIR Study. *Colloids Surfaces A Physicochem. Eng. Asp.* **2009**, *343*, 24–29.

(20) Swedlund, P. J.; Hamid, R. D.; Miskelly, G. M. Insights into H4SiO4 Surface Chemistry on Ferrihydrite Suspensions from ATR-IR, Diffuse Layer Modeling and the Adsorption Enhancing Effects of Carbonate. *J. Colloid Interface Sci.* **2010**, *352* (1), 149–157.

(21) Hiemstra, T. Ferrihydrite Interaction with Silicate and Competing Oxyanions: Geometry and Hydrogen Bonding of Surface Species. *Geochim. Cosmochim. Acta* **2018**, *238*, 453–476.

(22) Jordan, N.; Marmier, N.; Lomenech, C.; Giffaut, E.; Ehrhardt, J. J. Sorption of Silicates on Goethite, Hematite, and Magnetite: Experiments and Modelling. *J. Colloid Interface Sci.* **2007**, *312* (2), 224–229.

(23) Elgaroshi, S.; Miskelly, G. M.; Swedlund, P. J. H4SiO4 Sorption and Polymerization at the Magnetite - Aqueous Interface: The Influence of Interfacial Redox State. *Appl. Geochemistry* **2019**, *104*, 146–157.

(24) Xu, P.; Zeng, G. M.; Huang, D. L.; Feng, C. L.; Hu, S.; Zhao, M. H.; Lai, C.; Wei, Z.; Huang, C.; Xie, G. X.; Liu, Z. F. Use of Iron Oxide Nanomaterials in Wastewater Treatment: A Review. *Science of the Total Environment*. **2012**, *424*, 1–10.

(25) Gilbert, B.; Katz, J. E.; Denlinger, J. D.; Yin, Y.; Falcone, R.; Waychunas, G. A. Soft X-Ray Spectroscopy Study of the Electronic Structure of Oxidized and Partially Oxidized Magnetite Nanoparticles. *J. Phys. Chem. C* **2010**, *114* (50), 21994–22001.

(26) Gorski, C. A.; Nurmi, J. T.; Tratnyek, P. G.; Hofstetter, T. B.; Scherer, M. M. Redox Behavior of Magnetite: Implications for Contaminant Reduction. *Environ. Sci. Technol*. **2010**, *44* (1), 55–60.

(27) Cheng, W.; Marsac, R.; Hanna, K. Influence of Magnetite Stoichiometry on the Binding of Emerging Organic Contaminants. *Environ. Sci. Technol.* **2018**, *52* (2), 467–473.

(28) Latta, D. E.; Gorski, C. A.; Boyanov, M. I.; O'Loughlin, E. J.; Kemner, K. M.; Scherer, M. M. Influence of Magnetite Stoichiometry on U VI Reduction. *Environ. Sci. Technol.* **2012**, *46* (2), 778–786.

(29) Peterson, M. L.; White, A. F.; Brown, G. E.; Parks, G. A. Surface Passivation of Magnetite by Reaction with Aqueous Cr(VI): XAFS and TEM Results. *Environ. Sci. Technol.* **1997**, *31* (5), 1573–1576.

(30) Rovira, M.; Giménez, J.; Martínez, M.; Martínez-Lladó, X.; de Pablo, J.; Martí, V.; Duro, L. Sorption of Selenium(IV) and Selenium(VI) onto Natural Iron Oxides: Goethite and Hematite. *J. Hazard. Mater.* **2008**, *150* (2), 279–284.

(31) Jordan, N.; Ritter, A.; Scheinost, A. C.; Weiss, S.; Schild, D.; Hübner, R. Selenium(IV) Uptake by Maghemite (γ-Fe_2O_3). *Environ. Sci. Technol.* **2014**, *48* (3), 1665–1674.

(32) Duc, M.; Lefèvre, G.; Fédoroff, M. Sorption of Selenite Ions on Hematite. *J. Colloid Interface Sci.* **2006**, *298* (2), 556–563.

(33) Duc, M.; Lefevre, G.; Fedoroff, M.; Jeanjean, J.; Rouchaud, J. C.; Monteil-Rivera, F.; Dumonceau, J.; Milonjic, S. Sorption of Selenium Anionic Species on Apatites and Iron Oxides from Aqueous Solutions. *J. Environ. Radioact*. **2003**, 70, 61–72.

(34) Peak, D.; Sparks, D. L. Mechanisms of Selenate Adsorption on Iron Oxides and Hydroxides. *Environ. Sci. Technol.* **2002**, *36* (7), 1460–1466.

(35) Su, C.; Suarez, D. L. Selenate and Selenite Sorption on Iron Oxides An Infrared and Electrophoretic Study. *Soil Sci. Soc. Am. J.* **2000**, *64* (1), 101–111.

(36) Scheinost, A. C.; Kirsch, R.; Banerjee, D.; Fernandez-Martinez, A.; Zaenker, H.; Funke, H.; Charlet, L. X-Ray Absorption and Photoelectron Spectroscopy Investigation of Selenite Reduction by Fe^{II}-Bearing Minerals. *J. Contam. Hydrol.* **2008**, *102* (3–4), 228–245.

(37) Onoguchi, A.; Granata, G.; Haraguchi, D.; Hayashi, H.; Tokoro, C. Kinetics and Mechanism of Selenate and Selenite Removal in Solution by Green Rust-Sulfate. *R. Soc. Open Sci.* **2019**, *6* (4), 182147.

(38) Martínez, M.; Giménez, J.; De Pablo, J.; Rovira, M.; Duro, L. Sorption of Selenium(IV) and Selenium(VI) onto Magnetite. *Appl. Surf. Sci.* **2006**, *252* (10), 3767–3773.

(39) Scheinost, A. C.; Charlet, L. Selenite Reduction by Mackinawite, Magnetite and Siderite: XAS Characterization of Nanosized Redox Products. *Environ. Sci. Technol.* **2008**, *42* (6), 1984–1989.

(40) Kim, S. S.; Min, J. H.; Lee, J. K.; Baik, M. H.; Choi, J. W.; Shin, H. S. Effects of PH and Anions on the Sorption of Selenium Ions onto Magnetite. *J. Environ. Radioact.* **2012**, *104* (1), 1–6.

(41) Christl, I.; Brechbühl, Y.; Graf, M.; Kretzschmar, R. Polymerization of Silicate on Hematite Surfaces and Its Influence on Arsenic Sorption. *Environ. Sci. Technol.* **2012**, *46* (24), 13235–13243.

(42) Sugimoto, T.; Matijević, E. Formation of Uniform Spherical Magnetite Particles by Crystallization from Ferrous Hydroxide Gels. *J. Colloid Interface Sci.* **1980**, *74* (1), 227–243.

(43) Wojdyr, M. Fityk: A General-Purpose Peak Fitting Program. *J. Appl. Crystallogr.* **2010**, *43* (5 PART 1), 1126–1128.

(44) Doebelin, N.; Kleeberg, R. Profex: A Graphical User Interface for the Rietveld Refinement Program BGMN. *J. Appl. Crystallogr.* **2015**, *48* (5), 1573–1580.

(45) Teillet, J.; Varret, F.; Juraszek, J. MOSFIT Program. *MOSFIT program, unpublished*. Le Mans University France.

(46) Stöber, W.; Fink, A.; Bohn, E. Controlled Growth of Monodisperse Silica Spheres in the Micron Size Range. *J. Colloid Interface Sci.* **1968**, *26* (1), 62–69.

(47) Salgueiriño-Maceira, V.; Correa-Duarte, M. A.; Spasova, M.; Liz-Marzán, L. M.; Farle, M. Composite Silica Spheres with Magnetic and Luminescent Functionalities. *Adv. Funct. Mater.* **2006**, *16* (4), 509–514.

(48) Simonelli, L.; Marini, C.; Olszewski, W.; Ávila Pérez, M.; Ramanan, N.; Guilera, G.; Cuartero, V.; Klementiev, K. CLÆSS: The Hard X-Ray Absorption Beamline of the ALBA CELLS Synchrotron. *Cogent Phys.* **2016**, *3* (1), 1231987.

(49) Cornell, R. M.; Schwertmann, U. Crystal Structure. In *The Iron Oxides*; Wiley, 2003; pp 9–38.

(50) Gorski, C. A.; Scherer, M. M. Determination of Nanoparticulate Magnetite Stoichiometry by Mössbauer Spectroscopy, Acidic Dissolution, and Powder X-Ray Diffraction: A Critical Review. *Am. Mineral.* **2010**, *95* (7), 1017–1026.

(51) Gotić, M.; Koščec, G.; Musić, S. Study of the Reduction and Reoxidation of Substoichiometric Magnetite. *J. Mol. Struct.* **2009**, *924*, 347–354.

(52) Jubb, A. M.; Allen, H. C. Vibrational Spectroscopic Characterization of Hematite,

Maghemite, and Magnetite Thin Films Produced by Vapor Deposition. *ACS Appl. Mater. Interfaces* **2010**, *2* (10), 2804–2812.

(53) Fraga-García, P.; Schwaminger, S. P.; Berensmeier, S.; Bauer, D.; Wagner, F. E. Oxidation of Magnetite Nanoparticles: Impact on Surface and Crystal Properties. *CrystEngComm* **2016**, *19* (2), 246–255.

(54) Doriguetto, A. C.; Fernandes, N. G.; Persiano, A. I. C.; Filho, E. N.; Grenèche, J. M.; Fabris, J. D. Characterization of a Natural Magnetite. *Phys. Chem. Miner.* **2003**, *30* (5), 249–255.

(55) Daou, T. J.; Pourroy, G.; Bégin-Colin, S.; Grenèche, J. M.; Ulhaq-Bouillet, C.; Legaré, P.; Bernhardt, P.; Leuvrey, C.; Rogez, G. Hydrothermal Synthesis of Monodisperse Magnetite Nanoparticles. *Chem. Mater.* **2006**, *18* (18), 4399–4404.

(56) Toikka, G.; Hayes, R. A.; Ralston, J. Adhesion of Iron Oxide to Silica Studied by Atomic Force Microscopy. *J. Colloid Interface Sci.* **1996**, *180* (2), 329–338.

(57) Jolsterå, R.; Gunneriusson, L.; Holmgren, A. Surface Complexation Modeling of Fe_3O_4-H^+ and Mg(II) Sorption onto Maghemite and Magnetite. *J. Colloid Interface Sci.* **2012**, *386* (1), 260–267.

(58) Liang, X.; Wei, G.; Xiong, J.; Tan, F.; He, H.; Qu, C.; Yin, H.; Zhu, J.; Zhu, R.; Qin, Z.; Zhang, J. Adsorption Isotherm, Mechanism, and Geometry of Pb(II) on Magnetites Substituted with Transition Metals. *Chem. Geol.* **2017**, *470*, 132–140.

(59) Tamura, H.; Katayama, N.; Furuichi, R. Modeling of Ion-Exchange Reactions on Metal Oxides with the Frumkin Isotherm. 1. Acid-Base and Charge Characteristics of MnO_2, TiO_2, Fe_3O_4 and AI_2O_3 Surfaces and Adsorption Affinity of Alkali Metal Ions. *Environ. Sci. Technol.* **1996**, *30* (4), 1198–1204.

(60) Mayant, C.; Grambow, B.; Abdelouas, A.; Ribet, S.; Leclercq, S. Surface Site Density, Silicic Acid Retention and Transport Properties of Compacted Magnetite Powder. *Phys. Chem. Earth, Parts A/B/C* **2008**, *33* (14–16), 991–999.

(61) Catalette, H.; Dumonceau, J.; Ollar, P. Sorption of Cesium, Barium and Europium on Magnetite. *J. Contam. Hydrol.* **1998**, *35* (1–3), 151–159.

(62) Sun, Z.-X.; Su, F.-W.; Forsling, W.; Samskog, P.-O. Surface Characteristics of Magnetite in Aqueous Suspension. *J. Colloid Interface Sci.* **1998**, *197*, 151–159.

(63) Tamura, H.; Matijević, E.; Meites, L. Adsorption of Co^{2+} Ions on Spherical Magnetite Particles. *J. Colloid Interface Sci.* **1983**, *92* (2), 303–314.

(64) Wechsler, B. A., Lindsley. D. H., Prewitt, C. T. Crystal structure and cation distribution in titanomagnetites ($Fe_{3-x}Ti_xO_4$). *Am. Mineral*. **1984**, *69* (7-8), 754–770.

(65) Sjöberg, S. Silica in Aqueous Environments. *J. Non. Cryst. Solids* **1996**, *196*, 51–57.

(66) Ohmori, M.; Matijević, E. Preparation and Properties of Uniform Coated Colloidal Particles. VII. Silica on Hematite. *Colloid Interface Sci*. **1992**, *150* (2) 594–598.

(67) Osswald, J.; Fehr, K. T. FTIR Spectroscopic Study on Liquid Silica Solutions and Nanoscale Particle Size Determination. *J. Mater. Sci.* **2006**, *41* (5), 1335–1339.

(68) Bass, J. L.; Turner, G. L. Anion Distributions in Sodium Silicate Solutions. Characterization by ^{29}Si NMR and Infrared Spectroscopies, and Vapor Phase Osmometry. *J. Phys. Chem. B* **1997**, *101* (50), 10638–10644.

(69) Halasz, I.; Agarwal, M.; Li, R.; Miller, N. Vibrational Spectra and Dissociation of Aqueous Na_2SiO_3 Solutions. *Catal. Letters* **2007**, *117* (1–2), 34–42.

(70) Jamali-Behnam, F.; Najafpoor, A. A.; Davoudi, M.; Rohani-Bastami, T.; Alidadi, H.; Esmaily, H.; Dolatabadi, M. Adsorptive Removal of Arsenic from Aqueous Solutions Using Magnetite Nanoparticles and Silica-Coated Magnetite Nanoparticles. *Environ. Prog. Sustain. Energy* **2018**, *37* (3), 951–960.

(71) Marmier, N.; Delisée, A.; Fromage, F. Surface Complexation Modeling of Yb(III), Ni(II), and Cs(I) Sorption on Magnetite. *J. Colloid Interface Sci.* **1999**, *211* (1), 54–60.

(72) Cornell, R. M.; Schwertmann, U. Surface Chemistry and Colloidal Stability. In *The Iron Oxides*; Wiley, 2003; pp 221–252..

(73) Noh, J. S.; Schwarz, J. A. Estimation of the Point of Zero Charge of Simple Oxides by Mass Titration. *J. Colloid Interface Sci.* **1989**, *130* (1), 157–164.

(74) Kang, M.; Ma, B.; Bardelli, F.; Chen, F.; Liu, C.; Zheng, Z.; Wu, S.; Charlet, L. Interaction of Aqueous Se(IV)/Se(VI) with FeSe/FeSe2: Implication to Se Redox Process. *J. Hazard. Mater.* **2013**, *248–249* (1), 20–28.

(75) Cornell, R. M.; Schwertmann, U. Adsorption of Ions and Molecules. In *The Iron Oxides*; Wiley, 2003; pp 253–296.

(76) Sigg, L.; Stumm, W.; Berha, P. *Chimie Des Milieux Aquatiques. Paris, Masson.*; Dunod, 1992.

(77) Ma, B.; Fernandez-Martinez, A.; Madé, B.; Findling, N.; Markelova, E.; Salas-Colera, E.; Maffeis, T. G. G.; Lewis, A. R.; Tisserand, D.; Bureau, S.; Charlet, L. XANES-Based Determination of Redox Potentials Imposed by Steel Corrosion Products in Cement-Based Media. *Environ. Sci. Technol.* **2018**, *52* (20), 11931–11940.

(78) Fernández-Martínez, A.; Charlet, L. Selenium Environmental Cycling and Bioavailability: A Structural Chemist Point of View. *Reviews in Environmental Science and Biotechnology*. 2009, pp 81–110.

(79) Ma, B.; Fernandez-Martinez, A.; Wang, K.; Madé, B.; Hénocq, P.; Tisserand, D.; Bureau, S.; Charlet, L. Selenite Sorption on Hydrated CEM-V/A Cement in the Presence of Steel Corrosion Products: Redox vs Nonredox Sorption. *Environ. Sci. Technol.* **2020**, *54* (4), 2344–2352.

(80) Charlet, L.; Scheinost, A. C.; Tournassat, C.; Greneche, J. M.; Géhin, A.; Fernández-Martínez, A.; Coudert, S.; Tisserand, D.; Brendle, J. Electron Transfer at the Mineral/Water

Interface: Selenium Reduction by Ferrous Iron Sorbed on Clay. *Geochim. Cosmochim. Acta* **2007**, *71* (23), 5731–5749.

(81) Missana, T.; Alonso, U.; Scheinost, A. C.; Granizo, N.; García-Gutiérrez, M. Selenite Retention by Nanocrystalline Magnetite: Role of Adsorption, Reduction and Dissolution/Co-Precipitation Processes. *Geochim. Cosmochim. Acta* **2009**, *73* (20), 6205–6217.

(82) Hayes, K. F.; Roe, A. L.; Brown, G. E.; Hodgson, K. O.; Leckie, J. O.; Parks, G. A. In Situ X-Ray Absorption Study of Surface Complexes: Selenium Oxyanions on Agr-FeOOH. *Science* **1987**, *238* (4828), 783–786.

(83) Pearson, F. J.; Arcos, D.; Bath, A.; Boisson, J. Y.; Fernández, A. M.; Gäbler, H. E.; Gaucher, E.; Gautschi, A.; Griffault, L.; Hernán, P.; Waber, H. N. *Mont Terri Project – Geochemistry of Water in the Opalinus Clay Formation at the Mont Terri Rock Laboratory*; 2003; Vol. 10.

(84) Yanina, S. V.; Rosso, K. M. Linked Reactivity at Mineral-Water Interfaces Through Bulk Crystal Conduction. *Science*. **2008**, *320* (5873), 218–222.

(85) Alexandrov, V.; Rosso, K. M. Insights into the Mechanism of Fe(II) Adsorption and Oxidation at Fe-Clay Mineral Surfaces from First-Principles Calculations. *J. Phys. Chem. C* **2013**, *117* (44), 22880–22886.

(86) Latta, D. E.; Bachman, J. E.; Scherer, M. M. Fe Electron Transfer and Atom Exchange in Goethite: Influence of Al-Substitution and Anion Sorption. *Environ. Sci. Technol.* **2012**, *46* (19), 10614–10623.

(87) Maher, B. A.; Ahmed, I. A. M.; Karloukovski, V.; MacLaren, D. A.; Foulds, P. G.; Allsop, D.; Mann, D. M. A.; Torres-Jardón, R.; Calderon-Garciduenas, L. Magnetite Pollution Nanoparticles in the Human Brain. *Proc. Natl. Acad. Sci. U. S. A.* **2016**, *113* (39), 10797–10801.

SYNOPSIS. Mechanistic study about the redox reactivity of magnetite nanoparticles and selenium oxyanions in the presence and absence of silica coatings.